PNAS RESEARCH ARTICLE | APPLIED MATHEMATICS
BIOPHYSICS AND COMPUTATIONAL BIOLOGY

# Hemodynamic regulation allows stable growth of microvascular networks

Yujia Qi[a,1,2], Shyr-Shea Chang[b], Yixuan Wang[b,3], Cynthia Chen[c], Kyung In Baek[c], Tzung Hsiai[c,4], and Marcus Roper[b,d,1]

Edited by Patrick J. Drew, The Pennsylvania State University, University Park, PA; received June 29, 2023; accepted January 16, 2024 by Editorial Board Member Herbert Levine

**How do vessels find optimal radii? Capillaries are known to adapt their radii to maintain the shear stress of blood flow at the vessel wall at a set point, yet models of adaptation purely based on average shear stress have not been able to produce complex loopy networks that resemble real microvascular systems. For narrow vessels where red blood cells travel in a single file, the shear stress on vessel endothelium peaks sharply when a red blood cell passes through. We show that stable shear-stress-based adaptation is possible if vessel shear stress set points are cued to the stress peaks. Model networks that respond to peak stresses alone can quantitatively reproduce the observed zebrafish trunk microcirculation, including its adaptive trajectory when hematocrit changes or parts of the network are amputated. Our work reveals the potential for mechanotransduction alone to generate stable hydraulically tuned microvascular networks.**

vessel adaptation | microvessels | shear stress | endothelial wall | optimal networks

## Significance

Capillary beds need to equalize blood flows across hundreds or thousands of vessels. Here, we find that cues from the peak shear stresses alone are sufficient for the narrowest vessels to stably find their right radii. Our proposed adaptation principle can not only produce model zebrafish networks with uniform distribution of red blood cell flux but also predict the observed localization of blood flow when the global hematocrit changes, or when the distal artery–vein connection is removed. It reveals a function of artery–vein connections in regulating the development of uniform perfusive networks and advances uniform perfusion as an organizing principle for understanding microvascular network function and development.

Animal microvascular networks perfuse tissues with oxygen and glucose and remove waste. Since red blood cells almost fill the finest vessels, changes in vessel radius, even at the order of tenths of microns, can strongly alter vessel resistances and flows (1). The distribution of blood flows between vessels depends upon vessels finding their right radii.

The development and adaptation of vessels are conditional on blood flow information. Specifically, angiogenesis (2), specification of veins and arteries (3), and radius setting (4) are responsive to the wall shear stress induced by blood flow across a diverse array of animals and organs (3–11). Hydrodynamic stresses also control morphologies of many other kinds of biological transport networks, including slime mold plasmodia (12), fungal hyphae (13), and preferential flow paths in porous media biofilms (14).

Vascular radius regulation is achieved by endothelial cell migration (15) and changes in shape/orientation (4, 16) in response to shear stress. In particular, experimental evidence supports a fluid set point model, whereby endothelial cells attain a resting state only at a critical level of shear stress. When exposed to shear stresses above or below this set point, the endothelial cells exhibit an inflammatory response that resembles vascular remodeling (16) causing vessel radii to change over time to achieve the wall shear stress set point (16, 17).

Considerable theoretical work has tackled the question of how much of the complex geometries of real vascular networks can be recreated via models of shear stress adaptation. Shear stress adaptation can produce tree (i.e., loopless) networks that minimize the energy cost of delivering fluid from a source to multiple sinks (18, 19). However, shear stress set point models, as they have previously been analyzed, are incompatible with loopy networks, tending to produce structural instabilities in which parallel vessels are pruned down to simple paths (20).

A simple example shows the difficulty of programming robust network adaptation via shear stress set points. Consider the radius adaptation of a single vessel linking a source to a sink, under two scenarios: 1) The flow through the vessel is held constant, or 2) the pressure difference between the source and sink is held constant. In case (1), if the vessel radius increases, the shear stress will decrease. If, as is commonly assumed, vessel radius growth is triggered when shear stresses exceed the set point (18), the vessel's radius will converge to a fixed value. Conversely, in case (2), increasing the vessel's radius also increases the flow it carries, so increasing the radius of the vessel increases the shear stress on the vessel wall and set point triggered growth will continue without limit.

Here, we are motivated by observations of blood flow in the zebrafish embryo, for which there is direct evidence of shear-stress-dependent vessel remodeling (4, 16). At early stages of development, red blood cell flux is uniformly distributed across the fish trunk (21) but not at later stages when the hematocrit decreases (22). We focus specifically upon the narrowest and arguably, the most thoroughly studied (23)

The authors declare no competing interest.

This article is a PNAS Direct Submission. P.J.D. is a guest editor invited by the Editorial Board.



[1]To whom correspondence may be addressed. Email: qiyujia66@engineering.ucla.edu or mroper@math.ucla.edu.

[2]Present address: Department of Civil Chemical and Environmental Engineering, University of Genoa, Genova 16146, Italy.

[3]Present address: Department of Mathematics, University of Michigan, Ann Arbor, MI 48109.

[4]Present address: William H. Coulter Department of Biomedical Engineering, Georgia Institute of Technology and Emory University, Atlanta, GA 30322.

This article contains supporting information online at https://www.pnas.org/lookup/suppl/doi:10.1073/pnas.2310993121/-/DCSupplemental.

Published February 22, 2024.

microvessels, the trunk intersegmental vessels. Our model describes vessels that are narrow enough that cells may pass through them in a single file and so presents a mechanism of purely hemodynamic adaptation that could also stabilize other loopy networks formed by narrow vessels, such as capillary beds.

Previous mathematical models for stable network adaptation based purely on shear stresses have added flow unsteadiness by imposing fluctuations in the strengths of the sinks fed by the network (24, 25) or by opening and closing individual small vessels (18, 26). However, in the zebrafish embryo, there is no evidence of dynamic closing of intersegmental vessels. Models in which vessel radii respond to metabolic cues and inter-vessel signaling (20) or simply to local oxygen availability (27) can also stabilize loopy microvascular networks. Yet, at early stages of development, the thickness of the embryo is less than the Krogh length scale, so blood flow is not needed for oxygen transport, and embryos in hypoxic environments develop vasculatures that partition red blood cell flows as uniformly as normoxic fish (22).

The vascular system of the zebrafish trunk is a model system for vascular development (28) and has a particularly simple topology for study. It consists of an artery, the dorsal aorta (DA), and a vein, the principal cardinal vein (PCV) that are parallel to each other, connected directly by an anastomosis in the distal trunk (circled in the *Inset* of Fig. 1*A*) and indirectly via ladder-rung-like intersegmental vessels (Se-vessels) including intersegmental arteries (SeAs) and veins (SeVs) Fig. 1 *A* and *B* (29). Initially, the DA and PCV form a simple circulatory loop, from which SeAs and SeVs start to sprout at around 1.5 d post fertilization (dpf) (29). After extending dorsally, the sprouts form "T"s in the most dorsal regions of the trunk that extend rostrally and caudally, eventually anastomosing and then zippering together to form the dorsal longitudinal anastomotic vessels (DLAV), by 3.5 to 4 dpf (29). The Se vessels sprout even without blood flow in the DA and PCV, but in a wild-type embryo, flows are established in the intersegmental vessels by 2.5 d (30). Once circulation is established in the Se-vessels, hemodynamic stresses guide the specification of Se-vessels as veins and arteries by controlling the migration of venous endothelial cells into each nascent SeV (31).

We focus here on how the Se-arteries and veins find the right radii to receive uniform blood flows (*Results* and ref. 21). To achieve uniform blood flow between Se-vessels, vessel radii have to increase systematically and precisely from the head to the tail of the fish (21): Otherwise, the rostral intersegmental vessels would effectively short-circuit the trunk network, receiving greater flow than distal vessels (21, 32). In common with other animal microvascular networks, the diameters of the finest vessels in the zebrafish trunk are comparable to or smaller than the diameters of the red blood cells transported through them. Thus, the model of blood as a Newtonian or even, as a continuous non-Newtonian fluid, whose viscosity depends on vessel radius (33) misses the reality that shear stresses in real vessels are highly heterogeneous. In time, an endothelial cell (EC) experiences its largest wall shear stress at the moment that a red blood cell (RBC) passes. In this paper, we build a model from the hypothesis that endothelial cells respond to these peak shear stresses rather than average shear stress. We first analyze the mathematical properties of a model based on peak shear stresses, showing that peak shear stress responsive networks are stable and able to maintain loops. Then, we apply peak shear stress adaptation to the embryonic zebrafish trunk microvasculature. The peak shear stress model successfully produces uniform flows across intersegmental vessels, and, consistent with experiments, flow uniformity is temporarily lost during a period (7 to 14 d post fertilization) of decline in hematocrit. Finally, our model also highlights the indispensability of the direct anastomosis of artery and vein (Fig. 1 *A*, *Inset*) to allow the network to adapt to reach uniform flow, which we confirm experimentally by measuring intersegmental vessel flows following amputation of the anastomosis-containing distal trunk.

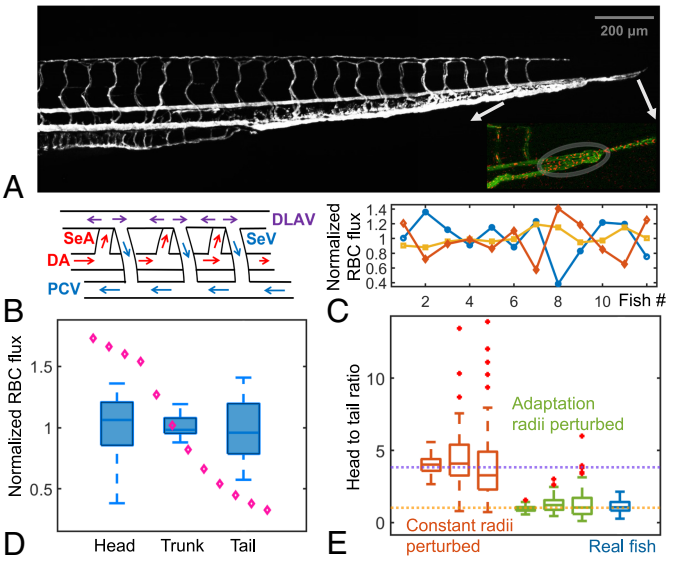


**Fig. 1.** Tuned vessel radii produce uniform intersegmental vessel flows in zebrafish embryos. (*A* and *B*) The trunk and tail of the zebrafish are perfused by a ladder-like network of microvessels, with inflow along the dorsal aorta (DA) and outflow along the posterior cardinal vein (PCV), along with a rung-like system of intersegmental arteries (SeAs) and veins (SeVs) linking the two vessels. (*A*) Composite angiogram of the trunk vessels in a 4-dpf embryo produced from images in the Zebrafish vascular atlas (29). DA and PCV are directly connected at the tail (*Inset*, shown in the circle); subtracting the background from phase contrast images makes red blood cells in this loop visible (*Inset*, red dots, *Materials and Methods*); superimposing 100 background subtracted images reveals the continuity of lumen through the loop (inset, green). (*B*) Simplified wiring diagram of a section of the trunk. (*C* and *D*) Individual 4-dpf fish have variable trunk flows but exhibit no bias in perfusion toward the rostral trunk. In (*C*), we plot RBC fluxes over distal, rostral, and mid-trunk SeAs among twelve 4-dpf individuals. Fluxes are normalized so that for each fish, the median flux across all SeAs is equal to 1. Each data point is pooled from 4 SeAs, in blue: distal (tail), red: rostral (head), and yellow: mid-trunk. (*D*) Pooling data from all fish shows no differences in fluxes between the three trunk regions. In comparison, a simulated model of the fish in which all SeAs are assigned the same radius (magenta dots) would have monotonically decreasing RBC flux from head to tail, due to the pressure gradient in the DA. (*E*) Flow uniformity requires tuning of vessel radii. We took constant (red boxes) and peak shear stress-adapted (green boxes) SeA radii (*Materials and Methods*), and perturbed the modeled radii of vessels by different percentages (10, 20, and 30 percent from *Left* to *Right*, 100 replicates of each), measuring the head to tail RBC flux ratios for each. The observed uniformity in real 4-dpf fish (blue box) is consistent with vessel radii being within 20% of their optimal values.

## Materials and Methods

**Measurement of Real Intersegmental RBC Flows.** We measured the RBC flow through each intersegmental artery (# / s) in 4- to 12-dpf (days post fertilization) zebrafish embryos, by imaging with 10× phase contrast and hand counting the number of RBCs passing pre-defined stations in each SeA. See *SI Appendix* for culturing and imaging conditions.

**A Peak Shear Stress Set Point Model.** We built a model in which vessel radius change is regulated by the fraction of endothelial cells (ECs) whose wall shear stress exceeds a set point. Importantly, we make this set point comparable to the peak wall shear stress. Blood flow in microvascular vessels is laminar (34, 35), though unsteady, due to the changing pressure in the artery that feeds them. We assume the Womersley number, *Wo*, measuring fluid acceleration, is low in all of our modeled networks (for zebrafish we obtain $Wo \sim 10^{-2}$ in DA,

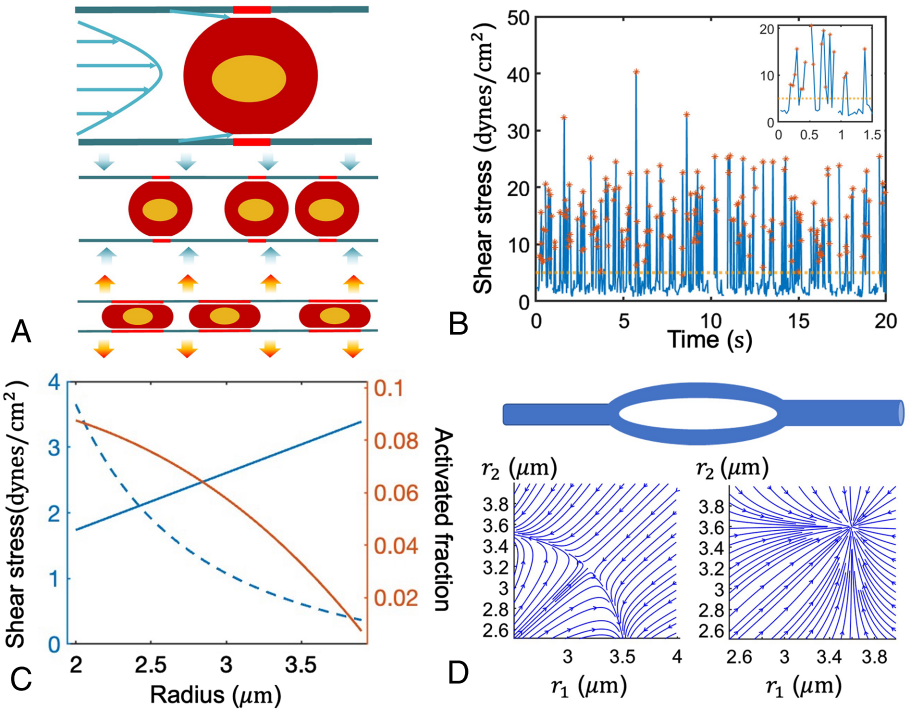


**Fig. 2.** Endothelial cells (ECs) experience heterogeneous shear stresses, peaking transiently when a red blood cell passes through the vessel, motivating us to model adaptation in response to peak shear stress (PSS). (*A*) *Upper*: RBCs deform and squeeze through the vessel, dragging on the ECs. We model a red blood cell as a cylinder with spherical ends and with fixed lubricating layer thickness $h = 0.1\,\mu$m. We divide the shear stress on the vessel wall into cell-free (Poiseuille-profile) and cell-touching (Couette-profile) regions and assume only the cell-touching regions exceed the shear stress set point. *Lower*: Schematic of PSS-adaptation. In wide vessels, RBCs are barely deformed, and a small fraction of ECs exceed the shear stress set point (red line portions of the vessel wall), while in narrow vessels, each highly deformed RBC causes a large RBC-EC contact area. Vessels with low and high PSS activations respectively shrink and grow (blue and orange arrows). (*B*) Calculated shear stresses on a single zebrafish SeA endothelial cell, based on our model of RBC-EC hydrodynamics applied to 20 s of RBC tracking data. Sharp spikes correspond to passages of an RBC (*Inset*: 1.5 s of data) and troughs to cell-free intervals. Only peak shear stresses exceed a typical threshold for shear-stress-induced EC remodeling (orange line, threshold taken from ref. 3). (*C*) PSS leads to a consistent decline in EC activation when vessel radius is increased, whether the inflow to the vessel is pressure or flow controlled (orange curve). By contrast, MSS-cues decrease in the vessel if its radius increases under constant flow (dashed blue) but increases under constant pressure (solid blue). (*D*) PSS activation stabilizes vessel geometries in a single parallel loop network (*Top* panel, schematic). The symmetric equilibrium is a saddle point under MSS adaptation (*Bottom-Left*)—the network tends to evolve to a state with one vessel pruned to flow. For PSS activation, the symmetric equilibrium is a stable node (*Bottom-Right*).

and $Wo \sim 10^{-3}$ in SeAs) (21), so flows respond effectively instantaneously to pressure changes and we consider a steady cardiac pressure, equal to the mean pressure of the real zebrafish heart. We model the hydraulic conductances of the vessels in the absence of RBCs by the Hagen–Poiseuille law (36). The inclusion of RBCs introduces two non-Newtonian effects to our model: 1, RBC filling of vessels increases their flow resistance and leads to heterogeneous wall shear stresses that peak when an RBC passes. 2, At vessel bifurcations, RBCs are governed by the Zweifach–Fung effect; they do not divide in the ratio of the flow rates but are more likely to enter vessels with higher blood flow (37–39).

Since RBCs move in single file in the microvessels that we model, we can divide each vessel into segments containing RBCs or not (Fig. 2 *A, Upper* panel), with respective shear stresses $\tau_{PSS}$ and $\tau_{NSS}$ (PSS stands for peak shear stress and NSS for null shear stress). For segments without RBCs, we calculate $\tau_{NSS}$ by assuming a Poiseuille (parabolic) velocity profile (36). RBCs become highly deformed during their single-file passage through a vessel (Fig. 2*A*), but are prevented from directly touching endothelial cells by a thin plasma lubricating layer with thickness $h$ which we assigned value 0.1 μm (Results were not sensitive to the value of $h$, *SI Appendix* Fig. S2*D*).

The shear stresses in the two regions are related to the mean velocity of flow, $U_i$, by formulae:

$$\tau_{NSS,i} = \frac{4\mu U_i}{r_i}\,,\quad \tau_{PSS,i} = \frac{\mu U_i}{h}\,, \qquad [1]$$

with $r_i$ the vessel radius and $\mu = 1 \times 10^{-6}$ g/(μm $s$) the dynamic viscosity of the plasma. From Eq. **1**, and experimental measurements of $U_i$, we obtained the time-varying wall shear stress at a representative point in a SeA, Fig. 2*B*.

For a SeA vessel $i$, of length $L$, containing $n_i$ RBCs, and with total pressure drop $\Delta P_i$, balancing forces gives:

$$\tau_{PSS,i} n_i (2\pi r_i l_i) + \tau_{NSS,i}(2\pi r_i (L - n_i l_i)) = \Delta P_i \pi r_i^2, \qquad [2]$$

where $l_i$ is the (deformed) length of each RBC, and $n_i$ can be related to vessel hematocrit $Ht_i$ by $n_i = Ht_i \cdot \pi r_i^2 L/(4/3 \cdot \pi R^3)$ . We use $R = 4\,\mu$m as the volumetric radius of a pre-deformed RBC. Undeformed zebrafish RBCs are ellipsoidal, with central bulges containing the nuclei. The precise shape of the contact region will rely on the elasticity of the RBC and its orientation. We model the salient features in a semi-quantitative way, with RBCs treated as spherical when undeformed, stretching into cylinders with spherical caps when squeezing through narrow vessels. Assuming $r_i \gg h$, so the lubricating layer thickness need not be considered when calculating RBC shape, the length of the cylindrical portion becomes $l_i = \frac{4}{3r_i^2}(R^3 - r_i^3)$. Assembling Eqs. **1** and **2**, we calculate the wall shear stress during RBC passage:

$$\tau_{PSS,i} = \mu \frac{U_i}{h} = \Delta P_i / \left( \frac{2 n_i l_i}{r_i} + \frac{8(L - n_i l_i)h}{r_i^2} \right) \qquad [3]$$

while the mean shear stress of the entire vessel is:

$$\tau_{MSS,i} = \frac{\Delta P_i \pi r_i^2}{2\pi r_i L} = \frac{\Delta P_i r_i}{2L} \qquad [4]$$

which is practically independent of the number of RBCs that it contains, given $\Delta P_i$ is insensitive in changes of hematocrit in SeAs (*SI Appendix*, Fig. S6).

When SeAs' hematocrit changes, the effect on wall shear stress is balanced by a reciprocal change in the velocity of RBCs to maintain $\tau_{MSS,i}$.

As with earlier works, we assume vessel radii adapt to shear stress cues. In previous works, the shear stress cue has been assumed to be the mean shear stress, $\tau_{MSS}$. We use this model as a point of comparison with our model, in which peak shear stresses, $\tau_{PSS}$, instead regulate adaptation. Specifically, our implementation of MSS-guided adaptation is:

$$\frac{dr_i}{dt} = C\left(\tau_{MSS,i} - \overline{\tau}_{MSS,i}\right)(r_i - r_{min}), \quad [5]$$

where $C$ is a constant representing the rate of adaptation, whose sign determines whether vessel radius increases ($C > 0$) or decreases ($C < 0$), when the shear stress set point $\overline{\tau}_{MSS}$ is exceeded. The factor $r_i - r_{min}$ establishes a minimum vessel radius: $r_{min} = R/2$. We prohibit RBCs from entering vessels for which $r_i = r_{min}$ (*SI Appendix*)).

Eq. **5** is compared with a model built for this work, in which peak shear stress, $\tau_{PSS}$, regulates vessel radius. Since shear stresses peak sharply during the passage of an RBC, we assume that the shear stress set point for each EC is exceeded when an RBC passes over it (Fig. 2*B*); so that a vessel's remodeling is regulated by the fraction of ECs that are in direct contact with RBCs. Specifically, we hypothesize:

$$\frac{dr_i}{dt} = C_1(f_i - \bar{f})(r_i - r_{min}). \quad [6]$$

$C_1 > 0$ is the rate of adaptation, $f_i$ is the fraction of stress-activated ECs, and $\bar{f}$ is a target fraction. We assign each SeA vessel the same target activation $\bar{f}$. Since $\tau_{PSS}$ is assumed to exceed the shear stress set point (Fig. 2*B*), the activation fraction $f_i$ is related to the number and length of RBCs within the vessel:

$$f_i = \frac{n_i l_i}{L} = Ht_i(1 - r_i^3/R^3). \quad [7]$$

Given the vessel radii, $r_i$, we first calculate the equilibrium number of RBCs, and thus the fraction of PSS-activated ECs, $f_i$, in each vessel by numerical relaxation. First, with an initial partitioning of RBCs between vessels, the vessel conductance, $\kappa_i \equiv \pi r_i^2 U_i/\Delta P_i$, can be obtained by combining Eqs. **1** and **2**:

$$\kappa_i = \frac{\pi r_i^4}{\mu(2n_i l_i r_i/h + 8(L - n_i l_i))}. \quad [8]$$

Using the conductance and boundary conditions, we can compute the whole blood flow into and out of each vessel by conserving flow at each bifurcation point. Assuming that each vessel is well mixed, and that by filling the vessel cross-section, red blood cells travel at the mean velocity of flow in the vessel, the flux of RBCs out of a vessel is set equal to $F_{i,out}dt$, where $F_{i,out} = Ht_i Q_i$ is the RBC flow rate, $Q_i$ is the flux of whole blood in the $i$-th SeA, and $dt$ is the relaxation time step. The flux into the vessel is $F_{i,in}dt$, computed from the flows and hematocrit of the DA vessel feeding into $i$-th vessel.

Compared to the outflows of RBCs for each SeA vessel, calculating the inflows $F_{i,in}$ requires more deliberate consideration. SeAs divert blood from a much larger vessel–the dorsal aorta (DA)–and RBCs are less likely to enter the SeAs than would be expected based on the ratio of flows, based on the Zweifach–Fung effect. Assuming the whole blood flow into the $i$-th SeA is $Q_i$, then the flow rate (no./time) of RBCs into the vessel is $F_{i,in} = C_{ZF,i}Ht_{i,DA}Q_i$, where $Ht_{i,DA}$ is the hematocrit of the upstream DA vessel directly feeding the $i$-th SeA, and the variable $C_{ZF,i}$ is the Zweifach–Fung factor for the $i$-th branching point. For simplicity of computation, we use a piecewise linear model for $C_{ZF,i}$ that is based on measurements of mammalian (un-nucleated) RBC partitioning at branching points (40, 41) (Fig. 3 *A* and *C*). To ensure mass conservation, the piecewise linear model is symmetric about $(K_{Q,i}, K_{F,i}) = (0.5, 0.5)$ (Fig. 3*A*, cyan broken line), where $K_{Q,i} = Q_i/Q_{i,DA}$, $K_{F,i} = F_{i,in}/F_{i,DA}$, and $Q_{i,DA}$ and $F_{i,DA}$ are respectively the whole blood flow and the RBC flux of the upstream DA vessel directly feeding the $i$-th SeA.

To be more precise, the Zweifach–Fung factor $C_{ZF,i}$ is decided by the fractional blood flow $K_{Q,i}$ at the $i$-th branching point based on the following piecewise linear equations (Fig. 3*A*),

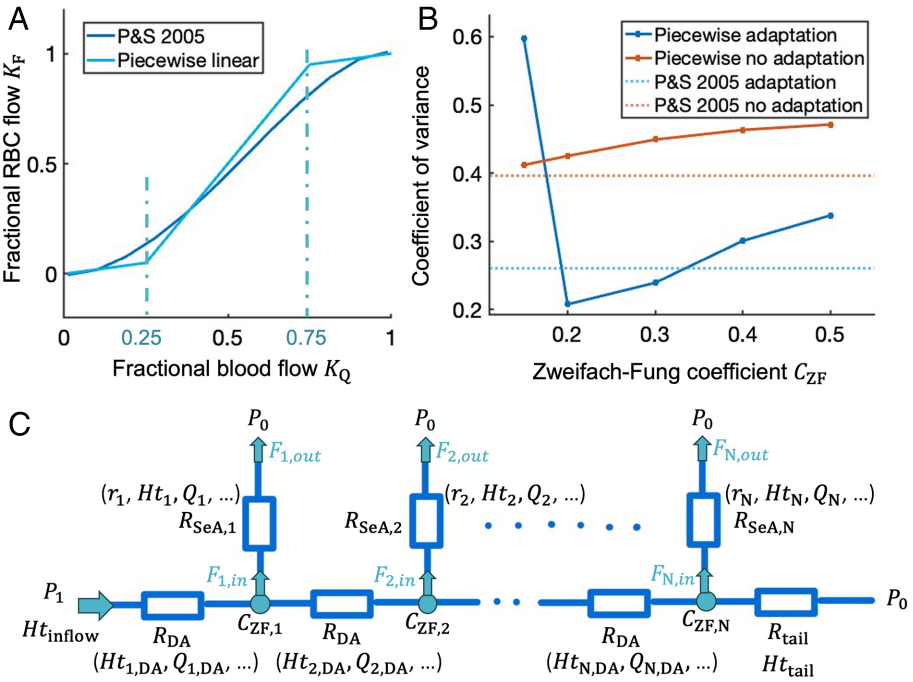


**Fig. 3.** Modeling the Zweifach–Fung effect (differential partitioning of RBCs from whole blood) is necessary to render flows in SeAs. (*A*) We assign a piecewise linear Zweifach–Fung factor to each branching point (cyan line), based on a simplification of the empirical equations in refs. 40 and 41 (blue line). Here, the x-axis represents the fraction of whole blood flux going into the SeAs at branching points, and the y-axis represents the fraction of RBC flux going into the corresponding SeA. The Zweifach–Fung factor $C_{ZF,i}$ is defined as the ratio between y and x values. (*B*) For 4-dpf fish with hematocrit 0.55, adaptation incorporating the Zweifach–Fung model reduces the coefficient of variance of RBC fluxes in SeAs (solid red line: $CV^2$, pre-adaptation, solid blue line: $CV^2$ post-adaptation) for a wide range of values for $C_{ZF}$. For comparison, we also show the pre- (dotted red) and post-adaptation (dotted blue) $CV^2$ values under the P&S 2005 model (40, 41). (*C*) A diagram of the model as a set of resistors. $R_{DA}$ and $R_{SeA,i}$ are, respectively, the flow resistance (the reciprocal of the flow conductance) for DA and the $i$-th SeA segments. At each branching point (circles), a Zweifach–Fung factor is decided based on the fractional blood flow entering the flowing SeA using the Zweifach–Fung model in *A*, and the total blood flow and RBC flux are conserved.

$$\begin{cases} K_{F,i} = C_{ZF} \cdot K_{Q,i}, & K_{Q,i} \in [0, 0.25] \\ K_{F,i} = (2 - C_{ZF})K_{Q,i} + 0.5(C_{ZF} - 1), & K_{Q,i} \in (0.25, 0.75] \\ K_{F,i} = C_{ZF}(K_{Q,i} - 1) + 1, & K_{Q,i} \in (0.75, 1] \end{cases}$$

and $C_{ZF,i}$ is defined as the ratio $K_{F,i}/K_{Q,i}$. Here $C_{ZF}$ is a constant Zweifach–Fung factor when the fraction of $Q_{i,DA}$ diverted into the SeA is small. We set $C_{ZF} = 0.2$, but different choices of $C_{ZF}$ do not qualitatively affect our results (Fig. 3*B*, blue lines). Notably, except when the tail is amputated, we find all of our SeAs operate in the regime where $C_{ZF,i} = C_{ZF}$. Where possible, we show that the empirical model of refs. 40 and 41, henceforth referred to as the P&S 2005 model, produces equivalent results (Fig. 3*B*).

At each time step, we update the number of RBCs, $n_i$, in each Se vessel based on the difference of $F_{i,in}$ and $F_{i,out}$, and update the number of RBCs in DA vessels by conserving RBC numbers at each bifurcation. We then recompute conductances and flows using Eq. **2**, continuing until all hematocrits and pressures at vessel branch points have converged. Convergence of these variables is not a true steady state: The locations of peak wall shear stresses vary as RBCs move, and wall shear stresses cycle with cardiac pressure. However, the spatial distribution of wall stresses is not needed to evolve vessel radii, and low *Wo* allows us to model time-averaged shear stresses. Additionally, since the DA has much larger conductance than the SeAs that it feeds (cf. ref. 42), time-varying partitioning of RBCs only weakly affects the junction pressures (*SI Appendix*, Fig. S6). Once flows and hematocrits have been computed, we update vessel radii, using an explicit discretization of Eq. **6**, and then recompute all hematocrits and flows. In the simulations shown here, we see two convergent states: $f_i \to \bar{f}$, or $r_i \to r_{min}$ (*SI Appendix*, Fig. S1).

For simplicity, we treat the network as symmetric, neglecting the Dorsal Longitudinal Anastomotic Vessel (DLAV), which divides the flow out of each SeA between two or even more SeVs. Hence, we need to model only the arteries and connect each SeA to an outlet with pressure $p_0 = 0$ (Fig. 3*C*). DA and PCV are also directly connected at the tail (Fig. 1 *A, Inset*). (Complete boundary and initial conditions are specified in *SI Appendix*, Table S1.) Note that $\bar{f}$ and $C_{ZF,i}$ decide the RBC flux collectively (*SI Appendix*, Fig. S2). However, for a wide range of parameters, adaptation always produces a more evenly distributed RBC flow for 4-dpf fish (*SI Appendix*, Fig. S2C).

## Results and Discussion

For a single vessel of radius $r$, with constant hematocrit, $Ht = 0.1$, we plot the mean shear stress $\tau_{MSS}$ according to Eq. **4** as a function of $r$, if the radius is changed while holding 1. the total flow or 2. the total pressure drop, constant. If flow rates are constant, then $\tau_{MSS}$ decreases with the vessel radius, whereas if the pressure drop is held constant, then the flow rate increases, so $\tau_{MSS}$ increases in proportion to the radius (Fig. 2*C*, blue dashed and solid curves respectively). Thus, no single model of the form Eq. **5** can stabilize vessel radii under both classes of boundary condition: For example, if $C > 0$, the vessel radius would converge under constant flow boundary conditions, but would diverge if the pressure drop were constant. Conversely, changing the sign of $C$ would stabilize the fixed pressure scenario, while destabilizing the fixed flow scenario. The same instability occurs when two unit-length vessels are arranged in a simple parallel network (Fig. 2 *D, Top*) with constant inflow into the network. If we assign the same target MSS, $\bar{\tau}_{MSS}$, to each vessel, there is one symmetric equilibrium with both vessels unpruned, i.e., $r_i = r^* > r_{min}$, but this equilibrium is a saddle point under Eq. **5**, under a broad class of conductance–radius relationships. For, if the conductance of the two vessels is $\kappa_i$, then each receives a portion $\frac{Q\kappa_i}{\kappa_1+\kappa_2}$ of the total inflow, and has MSS $\tau_i = \frac{Qr_i}{2(\kappa_1+\kappa_2)}$. Hence, at the equilibrium point, the Jacobian of Eq. **5** is:

$$J = C\,(r^* - r_{min}) \begin{bmatrix} \frac{\partial \tau_1}{\partial r_1} & \frac{\partial \tau_1}{\partial r_2} \\ \frac{\partial \tau_2}{\partial r_1} & \frac{\partial \tau_2}{\partial r_2} \end{bmatrix}$$

$$= \frac{CQ\,(r^* - r_{min})}{2(\kappa_1 + \kappa_2)^2} \begin{bmatrix} \kappa_1 + \kappa_2 - r_1 \frac{d\kappa_1}{dr_1} & -r_1 \frac{d\kappa_2}{dr_2} \\ -r_2 \frac{d\kappa_1}{dr_1} & \kappa_1 + \kappa_2 - r_2 \frac{d\kappa_2}{dr_2} \end{bmatrix}.$$

From which we obtain:

$$\det J = \frac{C^2 Q^2 (r^* - r_{min})^2}{4(\kappa_1 + \kappa_2)^3} \left( \kappa_1 - r_1 \frac{d\kappa_1}{dr_1} + \kappa_2 - r_2 \frac{d\kappa_2}{dr_2} \right).$$

For any model in which $\kappa_i$ is an increasing, convex function of $r_i$, with $\kappa(0) = 0$ (including Eq. **8**); $\kappa_i - r_i \frac{d\kappa_i}{dr_i} < 0$, so that $\det J < 0$, independently of the sign of $C$, making the equilibrium a saddle point. Indeed, any perturbation of the network from the equilibrium leads to one of the two vessels being pruned (Fig. 2*D*).

We calculated the shear stresses in a real zebrafish vessel (Fig. 2*B* shows the inferred stress given by Eq. **1**, for a representative EC). The pulses of high shear stress mark the passage of an RBC past the EC: We see that only during these pulses are stresses larger than thresholds typically identified for cellular remodeling (e.g., 5 dynes/cm$^2$ in ref. 43). We therefore propose that vessel remodeling is activated by the fraction of ECs at peak shear stress, or, equivalently, the fraction of time each EC spends at peak shear stress (Eq. **6**). Setting an activation threshold that exceeds the shear stress in normal plasma flow, we find the fraction of PSS activated ECs, $f$, decreases monotonically with vessel radius, both under conditions of constrained flow and of constrained pressure drop (Fig. 2*C*, orange curve), so that vessels remodeling according to Eq. **6** will converge in radius under both constant pressure or constant flow boundary conditions. Pairs of parallel vessels evolve to an equilibrium point where both of the vessels have the same conductances and flows (Fig. 2*D*).

**PSS-Activation Creates a Uniform Distribution of RBC Flux in Intersegmental Vessels.** For 4-dpf fish, we report the uniformity of RBC flux in Fig. 1. Consistent with previous measurements (21), we find that at 4-dpf, although there is significant variability in flows between different intersegmental vessels (Fig. 1 *C* and *D*), there is no systematic bias of flow toward either head or tail (Fig. 1*E*). The RBC fluxes in this and the following figures are normalized by the median flux in all SeA vessels, i.e., after normalization, the median flux is 1.

By contrast, if we copy the real zebrafish trunk microvasculature (*Materials and Methods*) but assign each SeA vessel the same radius, we predict that the head (proximal) SeA vessels will receive a flow that is 3.83 times greater than the tail (distal) vessels (Fig. 1*D*, purple dots). The amount of flow nonuniformity is smaller than that reported in ref. 32 because of the inclusion of the Zweifach–Fung effect in our model but is far greater than that observed in real zebrafish (median ratio for 12 fish: 1.0634, Fig. 1 *E*, boxes, *C* and *D*). To achieve a uniform RBC flow in SeAs, SeA radii have to increase from head to tail, to compensate for the decreasing pressure along the dorsal aorta (DA). Can Eq. **6** create a realistic zebrafish trunk vasculature? We first assigned each SeA a random radius between 3 and 4 μm and a same target fraction of PSS-activated ECs: $\bar{f}$, then evolved SeA vessel radii according to Eq. **6** using a piecewise linear Zweifach–Fung model to calculate RBC flows in each vessel. In the absence of vessel radius adaptation, we see a 4-fold decrease in flux from head (rostral) to tail (distal) SeAs (Fig. 4*A*), similar to when vessels were assigned identical radii (Fig. 1*D*). Fig. 4 *B* and *C* then show the trajectories of vessel radii and flows. When allowed to adapt according to Eq. **6**, SeA radii adapt to increase from head to tail (Fig. 4*C*). Since all RBC transits activate ECs,

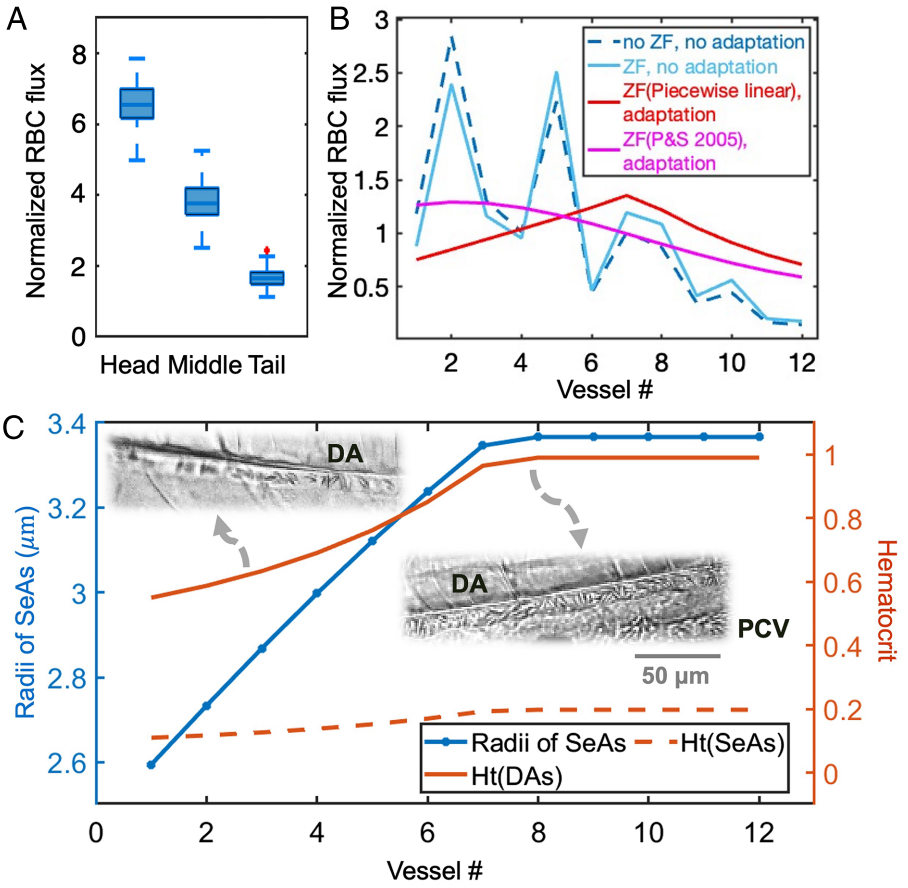


**Fig. 4.** PSS adaptation can robustly generate a model zebrafish microvascular network with 12 uniformly perfused SeAs. (*A*) Initial RBC fluxes (normalized so that median flux is 1) for 100 sets of random starting radii, with variance consistent with real zebrafish (Fig. 1*E*), give statistically decreasing RBC fluxes from head to tail. (*B*) Effect of modeled adaptation in a single fish with random initial radii. With (light blue solid) or without (blue dashed) the Zweifach–Fung effect, RBC fluxes are strongly biased toward the head. Evolving the vessel radii under Eq. **6** using either a piecewise linear or the P&S05 (40) model for the Zweifach Fung effect, produces more uniform RBC fluxes across all vessels (red and purple lines). (*C*) Uniformization of RBC fluxes is due to the interplay of radius tuning (blue curve) and the gradient of hematocrit, *Ht*, in the dorsal aorta that feeds each intersegmental vessel. *Ht* increases with distance along the DA (solid orange) until its saturation due to plasma skimming by SeAs (*Ht* in SeAs is shown by the dashed orange curve). *Insets* show experimental images of RBCs in two DA segments close to the head or tail. Distal SeAs respond to elevated *Ht* by growing wider rostral SeAs, compensating for decreasing pressure and uniformizing flows.

vessel radii are directly regulated by hematocrit, which increases from head to tail, due to the skimming of plasma from the DA by rostral SeAs, and saturates (i.e., hematocrit approaches 1) within the DA after the seventh vessel (Fig. 4*C*, orange curves). We confirmed the increase in hematocrit between rostral and distal DA in real 4-dpf zebrafish (Fig. 4 *C*, *Inset* images). Distal vessels grow wider in response to having higher RBC contact, compensating for the decreasing DA pressure (whose effect is evident in the pre-adaptation RBC flux distribution, Fig. 4*B*, blue line) and producing a more uniform partitioning of RBC fluxes (Fig. 4*B*). For the hematocrit-saturated SeAs in the caudal region, their radii cannot adapt in response to hematocrit changes, and the RBC flux in the caudal region decreases due to the decreasing DA pressure and thus a decreasing velocity of RBCs; however, an overall increase of SeA radii from head to tail is sufficient to balance the overall RBC flux distribution (Fig. 4*B*, red line). For the parameters chosen in Fig. 4, the ratio of fluxes in the 3 head-most SeAs to fluxes in the three tail-most SeAs is 1.03 after vessel radius adaptation, which is close to the observed value at 4 dpf (1.06).

We probed how close real SeA radii are to their optimal radii via a perturbation analysis. First, we created two model zebrafish trunks, one with all radii assigned equal values, and one with each vessel assigned its optimal radius calculated using the adaptation model. Then, we made replicate model fish, in which SeA radii were randomly perturbed by 10, 20, or 30% from either uniform or optimal radii (100 models each, for a total of 600 replicate models) and calculated the head-to-tail RBC flux ratio. We found that fluxes in real fish are consistent with all vessels being within 20% of their optimal radii (Fig. 1*E*).

Adaptation consistently uniformized flows across SeAs for a wide range of piecewise linear Zweifach–Fung models (obtained by varying the low whole blood flux value of $C_{ZF}$) (Fig. 3*B*) and for a heuristic phenomenological model with fluctuating $C_{ZF,i}$ (44), *SI Appendix*, Fig. S5. Similarly, results were not qualitatively changed when the piecewise linear model was replaced by an empirical model (P&S05) (40, 41). The P&S05 model rendered a smoother RBC flux distribution (magenta line in Fig. 4*B*) in which the DA did not reach saturating hematocrit (*SI Appendix*, Fig. S3), and with a slight head-to-tail decrease in fluxes (head to tail RBC flux ratio: 1.8). We noticed that when the input hematocrit varies, there is a shift in the location in the DA trunk where the hematocrit is predicted to saturate (*SI Appendix*, Fig. S4), changing which SeA receives the largest flow, which could explain why, although we observed no systematic bias of SeA flow toward the head or tail, in each fish, a different

portion of the trunk was greater perfused than the others (Fig. 1*C*). This observation motivates another question: During embryogenesis, hematocrit levels change by an order of magnitude (22): Is there a concurrent change in the partitioning of RBC fluxes?

**Uniform Perfusion Can Not Be Maintained When Hematocrit Decreases.** The stability of PSS-adaptation is conditional upon global hematocrit (*SI Appendix*, Fig. S4). During normal zebrafish development, there is a 3.5-fold decrease in hematocrit between 7 dpf and 15 dpf (22), potentially due to the transition from short-lived primitive RBCs to mature, oxygen-carrying RBCs (45). Concurrently, we observed a decrease of RBC flux in the rostral region during days 4 to 9 (64) and a complete absence of RBCs in the rostral region between days 10 and 12 (Fig. 5 *A* and *D*). Indeed, if hematocrit in a vessel decreases, then according to Eqs. **6** and **7** its radius will decrease to maintain the fraction, $\bar{f}$, of ECs in contact with RBCs. However, it may not be possible for a vessel to reach the target value of $\bar{f}$ before the radius reaches $r_{\min}$, cutting off the flow of RBCs into the vessel. SeA #1, by having the lowest hematocrit, is the most vulnerable to fail to achieve $\bar{f}$ (Fig. 4*C*, orange dash). The hematocrit in SeA #1 is always $Ht_1 = Ht_{\text{inflow}} C_{\text{ZF},1}$ after convergence ($Ht_{\text{inflow}}$ is the inflow hematocrit), based on our model for the Zweifach–Fung effect. For the vessel to reach its target fraction of PSS-activated ECs, based on Eq. **7**, we must have $Ht_{\text{inflow}} C_{\text{ZF},1}(1 - r_{\min}^3/R^3) > \bar{f}$, which we interpret as a constraint upon $Ht_{\text{inflow}} > Ht_{\min} = 0.457$, using the parameters in our model. When the hematocrit drops below this threshold, RBC flow ceases in SeA #1. Since the SeA continues to skim plasma from the DA, the DA supply to SeA #2 operates with higher hematocrit, but RBC flow also ceases in SeA #2 when $\frac{Q_{\text{inflow}} Ht_{\text{inflow}}}{Q_{\text{inflow}} - Q_1}$ drops below $Ht_{\min}$. We validate this analysis through numerical experiments: slowly decreasing $Ht_{\text{inflow}}$ in Eq. **6**, with the SeAs initially assigned uniform initial radii 3.5 μm. We initialize $Ht_{\text{inflow}} = 0.55 > Ht_{\min}$, for which the activation fraction model gives near uniform flow (Fig. 5*C*, blue circles). Decreasing $Ht_{\text{inflow}}$ to $0.45 < Ht_{\min}$, eliminates RBC flows in the first SeA (Fig. 5*B*). Plasma skimming by the first SeA means that the DA hematocrit reaching the second SeA (0.475) exceeds $Ht_{\min} = 0.457$, so the second and subsequent SeAs all remain perfused (Fig. 5 *B* and *C*, *Left Most* lines). All SeAs narrow from 2.6 to 3.4 μm radius to around 2.0 to 3.4 μm radius (the radii have an upper limit because of the saturation of the hematocrit). As we continue to decrease hematocrit, more rostral SeAs lose their RBC flux and become plasma skimmers (Fig. 5*C*, colored curves). Our predicted pattern is observed in real zebrafish (Fig. 5 *A* and *D*). The P&S05 model (40, 41) similarly produces a decreasing head-to-tail RBC flux ratio, though RBC flows do not stop in the rostral regions until 10 dpf, 2 d after cessation is observed in real zebrafish (Fig. 5*A*, purple line).

Continued PSS-remodeling is required to explain the loss of flow uniformity that co-occurs with decreasing hematocrit: If PSS-remodeling is stopped at 4 dpf, then, if we keep decreasing the input hematocrit, the head-to-tail RBC flux ratio decreases slightly and eventually converges to either 0.44 for the piecewise linear Zweifach–Fung model or 1.17 for the P&S05 model (Fig. 5*A*, dash lines), but the flow of RBCs through the rostral vessels does not cease.

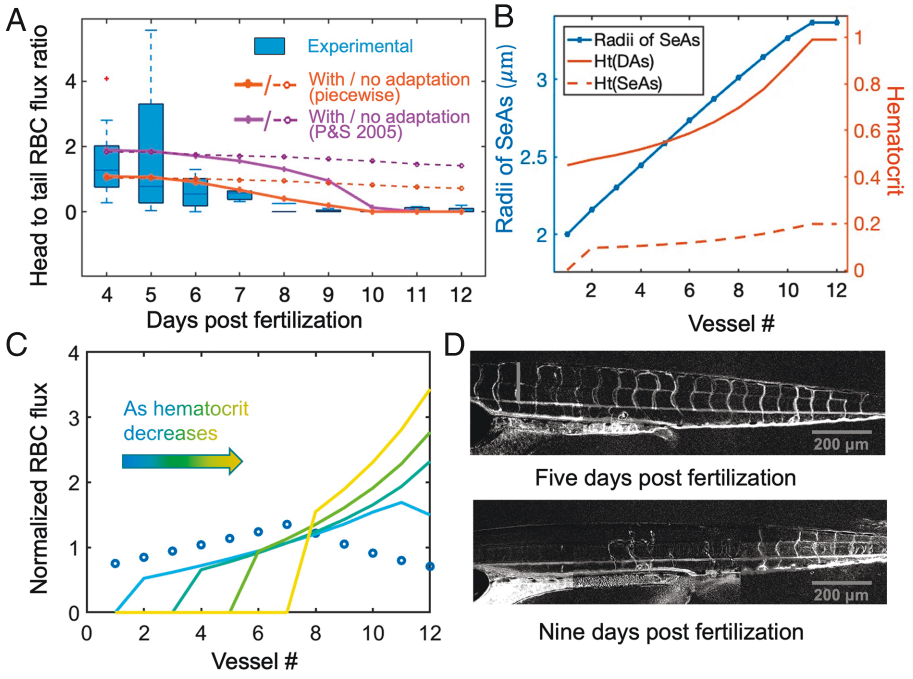


**Fig. 5.** Stable, uniform perfusion of the trunk is conditional upon hematocrit. (*A*) The ratio of RBC fluxes between the three most rostral and three most distal SeAs at each of 4 to 12 dpf ($N = 4$ fish for each day, each SeA measured for 30 s). The median head-to-tail RBC flux ratio decreases from day 4 to day 8, reaching 0 in 9 to 10 dpf, consistent with PSS adaptation (orange line). The P&S05 model (40, 41) produces a qualitatively similar result (purple line). If radius adaption stops at 4 dpf, the head-to-tail RBC flux ratio will never go to zero (orange and purple dash lines). For the adaptation models, the inflow hematocrit data are taken from ref. 22. (*B*) When hematocrit in the DA decreases below a critical threshold of 0.457, adaptation drives SeA #1 to its minimum radius. Plasma skimming keeps *Ht* above this threshold in the distal DA (solid red) and SeAs (dashed red). Radius adaptation (blue curve) creates a rostral–caudal gradient of radii and relatively uniform flow in the remaining perfused SeAs. (*C*) Simulated RBC fluxes under decreasing overall hematocrit, starting with an initial hematocrit of $Ht_{\text{inflow}} = 0.55$ (blue circles), and under decreasing $Ht_{\text{inflow}} = 0.45, 0.40, 0.35, 0.30$ (blue-yellow gradient). As hematocrit decreases, RBC fluxes vanish in an increasing number of rostral SeAs. (*D*) We superimpose a 30-s sequence of background-subtracted phase-contrast images (captured at 20 fps) of a 5-dpf (upper) and a 9-dpf (lower) fish. RBC fluxes across RBCs are uniform at 5 dpf. At 9 dpf, fluxes are eliminated in rostral SeAs but remain uniform in a subset of 7 caudal Se vessels.

Likewise, loss of flow uniformity due to changing hematocrit requires that vessel radii respond to peak rather than mean shear stresses. The DA has a much (~50 times) larger flow conductance than the SeAs. Thus, although hematocrit changes affect the absolute conductances of the vessels, blood pressures along the DA change little, given that cardiac activity is maintained from 4 to 14 dpf (46). As a result, pressure drops across each SeA are preserved. Changes in hematocrit do not therefore affect mean shear stresses on SeA vessel walls, and mean shear stress–induced remodeling does not produce the flow redistribution predicted by our model and seen in real zebrafish (*SI Appendix*, Fig. S6).

**Uniform Perfusion of the Trunk Is Dependent Upon Direct Anastomosis of the Artery and Vein.** Uniform perfusion of the trunk requires that SeA hematocrits increase with distance from the heart. Increasing hematocrit is possible because RBCs can remain in the DA, rather than entering an SeA. RBCs can even bypass the last SeA, since the DA and PCV are connected directly at the zebrafish tail (Fig. 1 *A, Inset*). Such arteriovenous anastomoses (also called shunts) are common in microcirculatory systems: Previously, we found that 12 out of 27 arterioles in a 2 $mm^3$ volume of sensory cortex, imaged in ref. 47, were directly connected to venules (48). Arteriovenous anastomoses have been hypothesized to contribute to pressure regulation and flow partitioning (49), or in the skin, in thermoregulation (50), but the understanding of their function remains incomplete. In the zebrafish embryo, sprouts from the DA–PCV loop develop into intersegmental vessels at 2 dpf (29) and, later, into caudal fin vascular plexus from 20 to 40 dpf (51), so the loop may not have a specific function in the intermediate aged fish studied here. Nonetheless, it diverts many (≈ 28%) of RBCs that pass through the trunk away from intersegmental vessels. We tested the hypothesis that the DA–PCV anastomosis contributes to flow uniformity across SeAs, by experimentally amputating the zebrafish tail following the methods described in ref. 52, and by running simulations of Eq. **6** with different conductances assigned to the DA–PCV anastomosis, including model networks in which the anastomosis was absent.

In our numerical study, the presence of the DA–PCV anastomosis ensured an equalized RBC flux across SeAs (Fig. 4*B*, purple and red lines). However, amputating the tail disrupts flow uniformity and produces large RBC flows in the distal unamputated SeAs. Allowing vessel radii to adapt to the new flows actually worsens flow localization to the tail (Fig. 6*A*, orange curve). Due to the Zweifach–Fung effect, SeA hematocrits are generally much smaller than the hematocrit of the DA segments that supply them. However, this effect can occur only when the total blood flow going into the SeA is smaller than the flow continuing along the DA (Fig. 3*A*). Without the DA–PCV anastomosis, there is no alternate path avoiding going into the most distal SeA, so the hematocrit in the last SeA must match the DA. Distal SeAs, therefore, have high hematocrits and flow rates. Radius adaptation then exacerbates flow localization since a large fraction of the most distal SeAs are PSS activated, cueing them to expand (e.g., from 3.36 to 3.80 μm for the last SeA), further increasing the portion of trunk RBC flow that they receive (Fig. 6*B*). Experimental observations of post-amputation flow support our quantitative predictions (64). Waiting 1 d post-amputation to allow bleeding to end and inflammation to diminish, we observed RBC flows far from and close to the amputation site

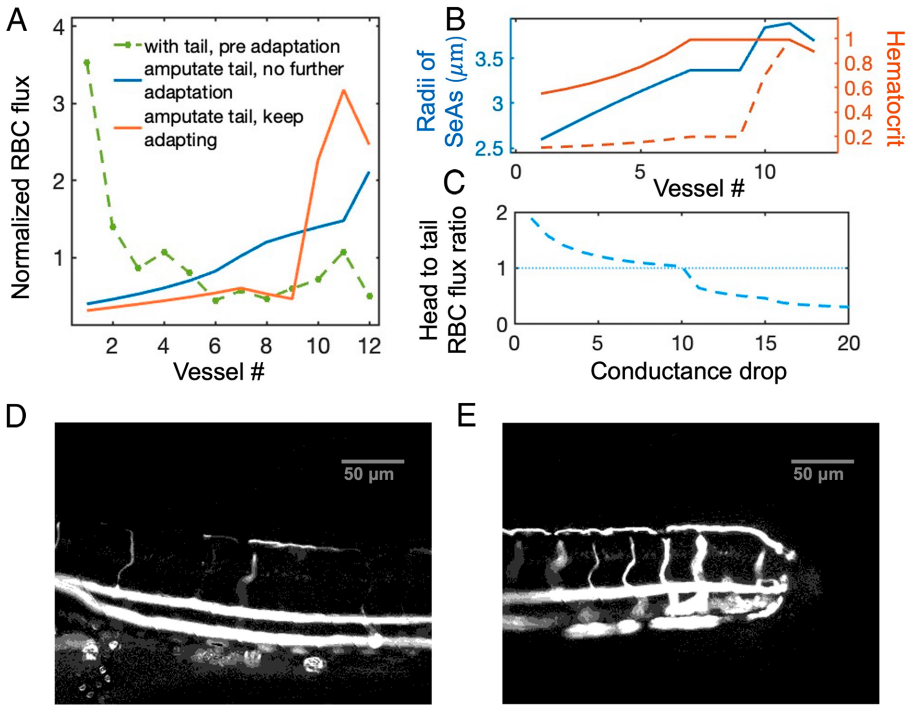


**Fig. 6.** Direct anastomosis between the dorsal artery (DA) and PCV is indispensable to ensuring uniform perfusion of intersegmental vessels. (*A*) Given random initial radii, we simulate RBC fluxes (normalized to have median 1) without the DA–PCV anastomosis before and after the adaptation of vessel radii. Removal of the tail causes a sharp spike in flux in the distal SeA (orange curve), compared with before adaptation (blue line and green dashes). (*B*) Following amputation, the predicted hematocrit level in distal SeAs spikes (orange dashed), though the DA hematocrit remains close to saturation (solid orange line). SeAs respond to increased perfusion by increasing their radii (blue line). (*C*) The conductance drop of the real DA–PCV loop from the DA (~6) is close to optimal for uniform perfusion. Here, we vary the conductance drop of the DA–PCV loop, compared to DA elements between SeAs. The head-to-tail RBC flux ratio decreases as the conductance drop is increased and is closest to 1 when the conductance drop is ~10. (*D* and *E*) Localization of blood flow is seen in a 5-dpf transgenic *Tg(fli1:eGFP; Gata1:ds-red)* zebrafish, 1-d post-amputation (methods from ref. 53). We superimpose DsRed channel data from 60 s of images, captured at a frame rate of 33 fps. Distal SeAs (*E*) have far greater RBC flux than rostral SeAs (*D*), due to a 1.87-fold increase in hematocrit.

(long exposure images are shown in Fig. 6 *D* and *E*). Hematocrit in the SeA closest to the amputation site is 3 to 10 fold larger than in rostral SeAs.

Numerically, we explore the effect of modulation of the conductance of the DA–PCV anastomosis by running adaptation simulations in replicate zebrafish in which the conductance of the DA–PCV anastomosis ranges from being equal to a segment of DA between two SeAs to being 20-fold smaller. When the anastomosis has the highest conductance, it diverts most RBCs from the SeAs, and RBC fluxes decrease from head to tail. If the anastomosis is made less conductive, the hematocrit in the last SeA increases, so adaptation decreases the head-tail ratio of fluxes. When the anastomosis conductance drop reaches 20 it is similar to a SeA segment. Then, similarly to amputation, distal SeAs receive more flow than rostral vessels (Fig. 6*C*, blue dash). Between these extremes, there is an optimal anastomosis conductance drop that matches head-to-tail RBC fluxes. The optimal conductance drop (∼7 to 10) matches what we observed in the real zebrafish (∼ 6).

## Conclusions

Our model for peak shear stress (PSS) activated vessel radius adaptation stably converges on model networks and leads to uniform perfusion of intersegmental vessels. PSS activation does not require that vessels be supplied with additional (e.g., metabolic) information, but it does mean that vessel remodeling is triggered in response to changes in hematocrit, consistently with our observations in 4- to 10-dpf zebrafish. In contrast, adaptation in response to mean shear stresses (MSS) can not produce stable loopy networks (20). Nor can MSS models predict the observed changes in flow partitioning that co-occur with hematocrit changes, since mean shear stresses are only mildly affected by the hematocrit decrease (*SI Appendix*, Fig. S6). Moreover, shear stresses known to be sufficient to induce cell remodeling, migration, and proliferation (3) greatly exceed measured MSS (54–56), implicating PSS in the adaptation of other animal microcirculatory networks.

We have focused exclusively upon tangential stresses: Radius-dependent blood cell sensing could potentially also be cued by circumferential stresses (57) or by the oxygen or ATP released by a single cell (58). However, by showing that hemodynamics alone can explain both network stability and adaptation dynamics, our model enlarges the applicability of the widely used model of shear stress points.

Large peak shear stresses occur in any narrow vessel through which red blood cells flow in a single file, including not only the intersegmental vessels considered here, but also capillaries. By contrast, we have not studied the adaptation of larger vessels such as the DA, for which hemodynamics are also known to play a radius setting role (4), and in which time-variation of shear stresses is dominated by blood flow pulsatility rather than by the passage of individual RBCs. Theoretical modeling has identified conditions under which pulsatile stresses alone may stabilize loopy networks (59) but has not yet been tested in real microvessels. In particular, we have not analyzed whether PSS activation is sufficient to stabilize the DA radius, and extending our model to DA-sized vessels would require new data about the radius-dependent blood rheology of zebrafish vessels (41).

In this work, we studied only how hematocrit changes affect vessel radius finding. We note that following zebrafish tail amputation, the altered flow in the most distal remaining SeA is a precursor both to the expansion of that vessel, as described here, and also to new vessel sprouting (52), implicating PSS-triggers in angiogenesis of narrow vessels. In comparison, in larger (20 to 100 μm diameter) vessels within the embryonic mouse yolk sac, sequestering erythrocytes prevented a hierarchical branching vascular network from developing. However, injecting hetastarch to increase plasma viscosity (60) rescued the hierarchical branching network, suggesting a separate role for whole blood mean shear stress in the angiogenesis of larger vessels.

In the zebrafish trunk, rostral SeAs decrease in radius and stop carrying RBCs when the whole organism's hematocrit is decreased. However, no SeA is permanently pruned; in our model, Eq. **6** enforces a minimum vessel radius, $r_{min}$. Rostral SeAs that approach this radius cease to carry RBCs but still participate in the circulation by plasma skimming from the DA, boosting its hematocrit, and enabling the network to find equilibria in which distal SeAs remain perfused by whole blood, consistent with experiments (Fig. 5 *C* and *D*). Conversely, in the embryonic zebrafish brain, reduction in blood flow is a precursor to complete vessel pruning (61), and wider application of our model would be helped by an understanding of the mechanisms that enforce minimum radii in some, but not all, vessels.

Modeling of the zebrafish trunk, confirmed by amputation experiments, shows that a direct connection between DA and PCV is indispensable to achieving uniform perfusion, and in the absence of this anastomosis, flows are severely localized to the most distal SeAs. The DA–PCV anastomosis plays roles early (1 dpf) and late (20 to 40 dpf) in development (29). Yet, since it diverts more than a quarter of RBCs that pass through the trunk away from the narrowest vessels, discussion of the anastomosis's costs and functions from 4 to 14 dpf should not be avoided. The presence of topologically similar vessels in the zebrafish hindbrain may provide additional evidence that AV anastomoses are functionally necessary during intermediate embryogenesis. The zebrafish hindbrain vasculature has the same ladder-rung layout as the trunk, with the basilar artery (rails) supplying parallel vertebral arteries (rungs). Similar to the DA–PCV loop, the basilar artery anastomoses directly with the rostral intersegmental vessels, allowing RBCs to circumvent the vertebral arteries (29). Interestingly, unlike the DA–PCV loop, the anastomosis is not present early in angiogenesis and is not needed to create a circulation-carrying loop prior to the formation of the vertebral arteries. Instead, the basilar artery is created by sprouts that develop from the primordial hind brain channels.

Our model provides theoretical guidance on creating loopy single-cell diameter networks with uniform flows via hemodynamic cues. Though our predictions are not dependent upon model details, data on the mechanics of RBC-vessel wall near contacts and the mechanics of RBCs dividing at vessel branching points (41) do not exist for the zebrafish microcirculation, and ongoing efforts to collect them will likely lead to a revision of the quantitative details. In particular, our model makes definitive predictions about the role played by the rostral–caudal gradient of hematocrit in the DA, predictions that are qualitatively supported by our observational data (Fig. 4*C*), and in quantitative accord with hematocrit gradient measurements in other organisms (62, 63). However, high-speed imaging of the DA would provide a quantitative test of the role of hematocrit differentials in uniformizing perfusion.

Finally, we note that although our model has been tested on the zebrafish microvascular network, uniformity of perfusion has emerged as an organizing principle in more topologically complex networks, such as the cortical vasculature (47, 48). Are hemodynamic cues sufficient to explain vessel organization and

radius finding in these networks? Importantly, in constructing our model networks, we assigned to each Se-vessel the same activation set point $\bar{f}$. In fact, shear stress set points can be minutely controlled via VEGFR3 expression levels. Whether, where, and how, this additional degree of freedom is used, will become clearer when the model is applied to emerging data streams for networks of single-cell diameter vessels.

**Data, Materials, and Software Availability.** Videos data have been deposited in Zenodo (https://doi.org/10.5281/zenodo.8354953) (64).

**ACKNOWLEDGMENTS.** We acknowledge financial support from National Institute of General Medical Sciences under award 5R01GM126556, and from the National Science Foundation, under grant under award DMS-2009317, and further support from a University of California, Los Angeles Dissertation Year Fellowship to S.-S.C. They also gratefully acknowledge the work of Yunxuan Li, who developed the first code for tracking red blood cells, and Clint Goodwin and Ariel Fitzmorris, who assisted with the manual tracking of cells. We also thank the anonymous reviewers, in particular, for one reviewer's detailed feedback on models for the Zweifach–Fung effect.

Author affiliations: [a]Department of Mechanical Engineering, University of California, Los Angeles, CA 90095; [b]Department of Mathematics, University of California, Los Angeles, CA 90095; [c]Department of Bioengineering, University of California, Los Angeles, CA 90095; and [d]Department of Computational Medicine, University of California, Los Angeles, CA 90095

Author contributions: Y.Q., S.-S.C., T.H., and M.R. designed research; Y.Q., S.-S.C., Y.W., C.C., and K.I.B. performed research; Y.Q. and S.-S.C. contributed new analytic tools; Y.Q. and S.-S.C. analyzed data; and Y.Q., S.-S.C., and M.R. wrote the paper.

1. T. Savin, M. Bandi, L. Mahadevan, Pressure-driven occlusive flow of a confined red blood cell. *J. Soft. Matter.* **12**, 562–573 (2016).
2. T. Zygmunt *et al*., 'In parallel' interconnectivity of the dorsal longitudinal anastomotic vessels requires both VEGF signaling and circulatory flow. *J. Cell Sci.* **125**, 5159–5167 (2012).
3. N. Baeyens *et al*., Vascular remodeling is governed by a VEGFR3-dependent fluid shear stress set point. *Elife* **4**, e04645 (2015).
4. W. W. Sugden *et al*., Endoglin controls blood vessel diameter through endothelial cell shape changes in response to haemodynamic cues. *Nat. Cell Biol.* **19**, 653–665 (2017).
5. H. H. Carter *et al*., Evidence for shear stress-mediated dilation of the internal carotid artery in humans. *Hypertension* **68**, 1217–1224 (2016).
6. A. Poduri *et al*., Endothelial cells respond to the direction of mechanical stimuli through SMAD signaling to regulate coronary artery size. *Development* **144**, 3241–3252 (2017).
7. B. Lowell Langille, F. O'Donnell, Reductions in arterial diameter produced by chronic decreases in blood flow are endothelium-dependent. *Science* **231**, 405–407 (1986).
8. U. Pohl, J. Holtz, R. Busse, E. Bassenge, Crucial role of endothelium in the vasodilator response to increased flow in vivo. *Hypertension* **8**, 37–44 (1986).
9. Z. Chen, E. Tzima, PECAM-1 is necessary for flow-induced vascular remodeling. *Arterioscler. Thromb. Vasc. Biol.* **29**, 1067–1073 (2009).
10. C. A. Franco *et al*., Dynamic endothelial cell rearrangements drive developmental vessel regression. *PLoS Biol.* **13**, e1002125 (2015).
11. L. John *et al*., The piezo1 cation channel mediates uterine artery shear stress mechanotransduction and vasodilation during rat pregnancy. *Am. J. Physiol. Heart Circ. Physiol.* **315**, H1019–H1026 (2018).
12. S. Marbach, N. Ziethen, L. Bastin, F. K. Bäuerle, K. Alim, Vein fate determined by flow-based but time-delayed integration of network architecture. *Elife* **12**, e78100 (2023).
13. L. Heaton *et al*., Analysis of fungal networks. *Fungal Biol. Rev.* **26**, 12–29 (2012).
14. D. L. Kurz *et al*., Competition between growth and shear stress drives intermittency in preferential flow paths in porous medium biofilms. *Proc. Natl. Acad. Sci. U.S.A.* **119**, e2122202119 (2022).
15. Y. Jin *et al*., Endoglin prevents vascular malformation by regulating flow-induced cell migration and specification through VEGFR2 signalling. *Nat. Cell Biol.* **19**, 639–652 (2017).
16. N. Baeyens, C. Bandyopadhyay, B. G. Coon, S. Yun, M. A. Schwartz, Endothelial fluid shear stress sensing in vascular health and disease. *J. Clin. Investig.* **126**, 821–828 (2016).
17. S. Rodbard, Vascular caliber. *Cardiology* **60**, 4–49 (1975).
18. H. Dan, D. Cai, Adaptation and optimization of biological transport networks. *Phys. Rev. Lett.* **111**, 138701 (2013).
19. H. Ronellenfitsch, E. Katifori, Global optimization, local adaptation, and the role of growth in distribution networks. *Phys. Rev. Lett.* **117**, 138301 (2016).
20. A. R. Pries, T. W. Secomb, P. Gaehtgens, Structural adaptation and stability of microvascular networks: Theory and simulations. *Am. J. Physiol. Heart Circ. Physiol.* **275**, H349–H360 (1998).
21. S.-S. Chang *et al*., Optimal occlusion uniformly partitions red blood cells fluxes within a microvascular network. *PLoS Comput. Biol.* **13**, e1005892 (2017).
22. T. Schwerte, D. Überbacher, B. Pelster, Non-invasive imaging of blood cell concentration and blood distribution in zebrafish Danio rerio incubated in hypoxic conditions in vivo. *J. Exp. Biol.* **206**, 1299–1307 (2003).
23. E. Ellertsdóttir *et al*., Vascular morphogenesis in the zebrafish embryo. *Dev. Biol.* **341**, 56–65 (2010).
24. F. Corson, Fluctuations and redundancy in optimal transport networks. *Phys. Rev. Lett.* **104**, 048703 (2010).
25. E. Katifori, G. J. Szöllősi, M. O. Magnasco, Damage and fluctuations induce loops in optimal transport networks. *Phys. Rev. Lett.* **104**, 048704 (2010).
26. H. Dan, D. Cai, A. V. Rangan, Blood vessel adaptation with fluctuations in capillary flow distribution. *PLoS One* **7**, e45444 (2012).
27. A. R. Pries, B. Reglin, T. W. Secomb, Structural adaptation of microvascular networks: Functional roles of adaptive responses. *Am. J. Physiol. Heart Circ. Physiol.* **281**, H1015–H1025 (2001).
28. N. D. Lawson, B. M. Weinstein, In vivo imaging of embryonic vascular development using transgenic zebrafish. *Dev. Biol.* **248**, 307–318 (2002).
29. S. Isogai, M. Horiguchi, B. M. Weinstein, The vascular anatomy of the developing zebrafish: An atlas of embryonic and early larval development. *Dev. Biol.* **230**, 278–301 (2001).
30. S. Isogai, N. D. Lawson, S. Torrealday, M. Horiguchi, B. M. Weinstein, Angiogenic network formation in the developing vertebrate trunk. *Development* **130**, 5281–5290 (2003).
31. B. Weijts *et al*., Blood flow-induced notch activation and endothelial migration enable vascular remodeling in zebrafish embryos. *Nat. Commun.* **9**, 5314 (2018).
32. S.-S. Chang, M. Roper, Microvascular networks with uniform flow. *J. Theor. Biol.* **462**, 48–64 (2019).
33. A. R. Pries, T. W. Secomb, P. Gaehtgens, J. F. Gross, Blood flow in microvascular networks. Experiments and simulation. *Circ. Res.* **67**, 826–834 (1990).
34. E. Today, Jay R Hove. In vivo biofluid dynamic imaging in the developing zebrafish. *Birth Defects Res. Part C Rev.* **72**, 277–289 (2004).
35. E. A. V. Jones, F. le Noble, A. Eichmann, What determines blood vessel structure? Genetic prespecification vs. hemodynamics. *Physiology* **21**, 388–395 (2006).
36. D. J. Acheson, *Elementary Fluid Dynamics* (Oxford University Press, 1990).
37. J. W. Dellimore, M. N. Dunlop, P. B. Canham, Ratio of cells and plasma in blood flowing past branches in small plastic channels. *Am. J. Physiol. Heart Circ. Physiol.* **244**, H635–H643 (1983).
38. B. M. Fenton, R. T. Carr, G. R. Cokelet, Nonuniform red cell distribution in 20 to 100 μm bifurcations. *Microvasc. Res.* **29**, 103–126 (1985).
39. A. R. Pries, K. Ley, M. Claassen, P. Gaehtgens, Red cell distribution at microvascular bifurcations. *Microvasc. Res.* **38**, 81–101 (1989).
40. A. R. Pries, T. W. Secomb, Microvascular blood viscosity in vivo and the endothelial surface layer. *Am. J. Physiol. Heart Circ. Physiol.* **289**, H2657–H2664 (2005).
41. T. W. Secomb, Blood flow in the microcirculation. *Annu. Rev. Fluid Mech.* **49**, 443–461 (2017).
42. D. Obrist, B. Weber, A. Buck, P. Jenny, Red blood cell distribution in simplified capillary networks. *Philos. Trans. Royal Soc. A.: Math. Phys. Eng. Sci.* **368**, 2897–2918 (2010).
43. N. Baeyens *et al*., Syndecan 4 is required for endothelial alignment in flow and atheroprotective signaling. *Proc. Natl. Acad. Sci. U.S.A.* **111**, 17308–17313 (2014).
44. A. Merlo *et al*., A few upstream bifurcations drive the spatial distribution of red blood cells in model microfluidic networks. *J. Soft Matter* **18**, 1463–1478 (2022).
45. B. M. Weinstein *et al*., Hematopoietic mutations in the zebrafish. *Development* **123**, 303–309 (1996).
46. E. Jacob, M. Drexel, T. Schwerte, B. Pelster, Influence of hypoxia and of hypoxemia on the development of cardiac activity in zebrafish larvae. *Am. J. Physiol. Integr. Comp. Physiol.* **283**, R911–R917 (2002).
47. P. Blinder *et al*., The cortical angiome: An interconnected vascular network with noncolumnar patterns of blood flow. *Nat. Neurosci.* **16**, 889–897 (2013).
48. Y. Qi, M. Roper, Control of low flow regions in the cortical vasculature determines optimal arterio-venous ratios. *Proc. Natl. Acad. Sci. U.S.A.* **118**, e2021840118 (2021).
49. J. L. Sherman Jr., Normal arteriovenous anastomoses. *Medicine* **42**, 247–268 (1963).
50. L. Walløe, Arterio-venous anastomoses in the human skin and their role in temperature control. *Temperature* **3**, 92–103 (2016).
51. C. Huang *et al*., Collagen ix is required for the integrity of collagen ii fibrils and the regulation of vascular plexus formation in zebrafish caudal fins. *Dev. Biol.* **332**, 360–370 (2009).
52. K. I. Baek *et al*., Vascular injury in the zebrafish tail modulates blood flow and peak wall shear stress to restore embryonic circular network. *Front. Cardiovasc. Med.* **9**, 841101 (2022).
53. M. Roustaei *et al*., Computational simulations of the 4D micro-circulatory network in zebrafish tail amputation and regeneration. *J. R. Soc. Interface* **19**, 20210898 (2022).
54. E. Roux, P. Bougaran, P. Dufourcq, T. Couffinhal, Fluid shear stress sensing by the endothelial layer. *Front. Physiol.* **11**, 861 (2020).
55. J. A. Kornuta *et al*., Effects of dynamic shear and transmural pressure on wall shear stress sensitivity in collecting lymphatic vessels. *Am. J. Physiol. Integr. Comp. Physiol.* **309**, R1122–R1134 (2015).
56. J. Brandon Dixon *et al*., Lymph flow, shear stress, and lymphocyte velocity in rat mesenteric prenodal lymphatics. *Microcirculation* **13**, 597–610 (2006).
57. A. R. Pries, T. W. Secomb, Control of blood vessel structure: Insights from theoretical models. *Am. J. Physiol. Heart Circ. Physiol.* **288**, H1010–H1015 (2005).
58. M. L. Ellsworth, The red blood cell as an oxygen sensor: What is the evidence? *Acta Physiol. Scand.* **168**, 551–559 (2000).
59. P. Chatterjee, S. Fancher, E. Katifiori, Pulsatile driving stabilizes loops in elastic flow networks. arXiv [Preprint] (2022). http://arxiv.org/abs/2210.06557 (Accessed 1 May 2023).
60. J. L. Lucitti *et al*., Vascular remodeling of the mouse yolk sac requires hemodynamic force. *Development* **134**, 3317–3326 (2007).
61. Q. Chen *et al*., Haemodynamics-driven developmental pruning of brain vasculature in zebrafish. *PLoS Biol.* **10**, e1001374 (2012).
62. N. D. Mylniczenko, E. W. Curtis, R. E. Wilborn, F. A. Young, Differences in hematocrit of blood samples obtained from two venipuncture sites in sharks. *Am. J. Vet. Res.* **67**, 1861–1864 (2006).
63. K. L. Arora *et al*., Differences in hemoglobin and packed cell volume in blood collected from different sites in Japanese quail (Coturnix japonica). *Int. J. Poult. Sci.* **9**, 828–830 (2010).
64. Y. Qi, zebrafish bloodflow. Zenodo. https://doi.org/10.5281/zenodo.8354953. Deposited 18 September 2023.